Contents lists available at ScienceDirect

Nuclear Instruments and Methods in Physics Research B

Quantum primary rainbows in transmission of positrons through very short carbon nanotubes

M. Ćosić *, S. Petrović, N. Nešković

Laboratory of Physics, Vinča Institute of Nuclear Sciences, University of Belgrade, P.O. Box 522, 11001 Belgrade, Serbia

ABSTRACT

This paper is devoted to a quantum mechanical consideration of the transmission of positrons of a kinetic energy of 1 MeV through very short (11, 9) single-wall chiral carbon nanotubes. The nanotube lengths are between 50 and 320 nm. The transmission process is determined by the rainbow effects. The interaction potential of a positron and the nanotube is deduced from the Molire's interaction potential of the positron and a nanotube atom using the continuum approximation. We solve numerically the time-dependent Schrödinger equation, and calculate the spatial and angular distributions of transmitted positrons. The initial positron beam is assumed to be an ensemble of non-interacting Gaussian wave packets. We generate the spatial and angular distributions using the computer simulation method. The examination is focused on the spatial and angular primary rainbows. It begins with an analysis of the corresponding classical rainbows, and continues with a detailed investigation of the amplitudes and phases of the wave functions of transmitted positrons. These analyses enable one to identify the principal and supernumerary primary rainbows appearing in the spatial and angular distributions. They also result in a detailed explanation of the way of their generation, which includes the effects of wrinkling of each wave packet during its deflection from the nanotube wall, and of its concentration just before a virtual barrier lying close to the corresponding classical rainbow. The wrinkling of the wave packets occurs due to their internal focusing. In addition, the wave packets wrinkle in a mutually coordinated way. This explanation may induce new theoretical and experimental investigations of quantum rainbows occurring in various atomic collision processes.

© 2016 Elsevier B.V. All rights reserved.

1. Introduction

A positively charged particle is considered as being channeled if it is undergoing a series of correlated small angle collisions with the atoms of the atomic strings defining an axial or planar channel of a crystal [1–3]. The maxima of the yield of particles transmitted through the channel occurring due to the singularities of the mapping of the impact parameter plane to the final transverse position plane or transmission angle plane are called rainbows [4–8]. In accordance with that, the process in which such maxima appear is referred to as rainbow channeling. If the particle kinetic energy is sufficiently high to make the quantum aspects of its behavior negligible, the maxima are called classical rainbows. On the other hand, when the particle kinetic energy is sufficiently low to make the quantum effects dominant, the maxima are designated as quantum rainbows. Each quantum rainbow comprises a principal rainbow and one or more supernumerary rainbows.

Carbon nanotubes are the sheets of carbon atoms lying at the hexagonal crystal lattice sites rolled up into cylinders [9–11]. If the atomic strings of a nanotube spiral around its axis, it is called chiral, and if the atomic strings are parallel to the axis, it is called achiral. Nanotubes can be the single-wall and multi-wall ones, depending on the number of cylinders they contain. The nanotube diameters are of the order of a nanometer and their lengths can be more than a hundred micrometers.

Carbon nanotubes can be used to channel positively charged particles [12]. So far, a number of theoretical groups have studied ion channeling in nanotubes with the main objective to explore the possibility of guiding ion beams with nanotubes [13]. On the other hand, it has been established that rainbows appear in channeling of charged particles in nanotubes as well [14–17]. The experimental studying of ion channeling in nanotubes has not yet been sufficiently developed [18,,19].

Recently, Petrović et al. [17] presented a classical and quantum mechanical investigation of the transmission of positrons through very short (11, 9) single-wall chiral carbon nanotubes. The positron kinetic energies were 1 and 10 MeV while the nanotube lengths

* Corresponding author.
  E-mail address: mcosic@vinca.rs (M. Ćosić).

were 200 and 560 nm, respectively. The analysis was focused on the rainbow effects, which were clearly observed in the spatial and angular distributions of transmitted positrons. The quantum rainbow maxima were explained by the constructive interference of the two rays within the wave packet that started from the points in the impact parameter plane on the two sides of the rainbow point and finished at the same point in the final transverse position plane or transmission angle plane. These authors have used the same approach to explore the possibility of using quantum rainbows for characterization of very short carbon nanotubes [20].

Here, we present a detailed quantum mechanical study of the transmission of positrons of a kinetic energy of $E = 1$ MeV through very short (11, 9) single-wall chiral carbon nanotubes. The nanotube lengths are $L = 50$–320 nm. The corresponding reduced nanotube lengths are $\Lambda = 0.03$–0.19 [5,6,17]. The initial positron beam is taken to be divergent relative to the nanotube axis. Its full-width-at-half-maximum (FWHM) is denoted as Δ_d. The equilibrium nanotube radius is $R_n = 0.69$ nm [10]. The study is a continuation of the studies of Petrović et al. [17] and Ćosić *et al.* [20]. It is focused on the quantum primary rainbows, *i.e.*, the principal and supernumerary primary rainbows, occurring in the spatial and angular distributions of transmitted positrons. We present a detailed analysis of the amplitudes and phases of the wave functions of transmitted positrons, and give a quantum mechanical explanation of the obtained distributions.

2. Theory

The subject of this study is a positron channeled in a nanotube. We choose the z axis to coincide with the nanotube axis; it is the longitudinal axis. The x and y axes are taken to be the vertical and horizontal axes, respectively; they are the transverse axes. The origin lies in the nanotube entrance plane. The nanotube entrance plane is the positron impact parameter plane, the nanotube exit plane is its final transverse position plane, and a plane in between them is a transverse position plane.

2.1. Interaction potentials

In order to describe the interaction of the positron and a nanotube atom, we use the Molière's interaction potential [21]. The needed interaction potential of the positron and nanotube is deduced in three steps. In the first step, we axially average the positron-atom interaction potential, employing the continuum approximation [2]. In the second step, the interaction potential obtained in the first step is azimuthally averaged. This is justified by the facts that the nanotube is chiral and contains even 602 pairs of atomic strings parallel to its axis. The resulting positron-nanotube interaction potential reads

$$U(\rho; R_n) = U_0 \sum_{i=1}^{3} \alpha_i K_0 \left(\frac{\beta_i R_n}{a_s}\right) I_0 \left(\frac{\beta_i \rho}{a_s}\right) \quad \text{for} \quad \rho \leqslant R_n \tag{1}$$

and

$$U(\rho; R_n) = U_0 \sum_{i=1}^{3} \alpha_i I_0 \left(\frac{\beta_i R_n}{a_s}\right) K_0 \left(\frac{\beta_i \rho}{a_s}\right) \quad \text{for} \quad \rho > R_n \tag{2}$$

with

$$U_0 = \frac{16\pi Z_2 e^2 R_n}{3^{3/2} a_b^2}, \tag{3}$$

where $Z_2 = 6$ is the nanotube atom atomic number, e is the elementary charge, $a_s = [9\pi^2/(128Z_2)]^{1/3} a_0$ is the nanotube atom screening radius with $a_0 = 0.026$ nm being the Bohr radius, $a_b = 0.14$ nm is

the nanotube atoms bond length [10], $\rho = (x^2 + y^2)^{1/2}$ with x and y being the transverse components of the positron position vector, $(\alpha_i) = (0.35, 0.55, 0.10)$ and $(\beta_i) = (0.1, 1.2, 6.0)$ are the fitting parameters, and I_0 and K_0 denote the modified Bessel functions of the first and second kinds and 0th order, respectively [22]. The Molière's interaction potential with the above given screening radius is chosen because it was employed for a very successful reproduction of a rainbow channeling experiment with an accurate computer simulation code [23]. It is evident that Eqs. (1)–(3) do not contain explicitly the nanotube chiral indices, $m = 11$ and $n = 9$. These indices are hidden in $R_n = [(3^{1/2}/(2\pi)](m^2 + mn + n^2)^{1/2} a_b$ [22].

In the third step, we introduce the thermal vibrations of nanotube atoms [24,17]. This is done in a way appearing as the averaging of the interaction potential obtained in the second step over the effective thermally induced changes of the nanotube radius, R, from its equilibrium value, R_n, along the ρ axis. The positron-nanotube interaction potential is given by

$$U_{th}^{qu}(\rho; R_n) = \frac{1}{(2\pi)^{1/2} \sigma_{th}} \int_{R_1}^{R_2} U(\rho; R) \exp\left[-\frac{(R - R_n)^2}{2\sigma_{th}^2}\right] dR, \tag{4}$$

where $\sigma_{th} = 0.0053$ nm [25] is the one-dimensional thermal vibration amplitude of the nanotube atoms. We take that the integration limits appearing in this expression are $R_1 = R_n - 6\sigma_{th}$ and $R_2 = R_n + 6\sigma_{th}$. They determine the interval in which the changes of the integrand are not negligible. The integration is performed numerically. It should be emphasized that the function $U_{th}^{qu}(\rho; R_n)$ and its first derivative are continuous. However, if one takes into account the fact that the displacements of the nanotube atoms are small, a useful analytical approximation of Eq. (4) can be derived [16,17]. When $\rho \leqslant R_n$, this equation becomes

$$U_{th}^{cl}(\rho; R_n) = U_0 \sum_{i=1}^{3} \left(\alpha_i + \frac{\sigma_{th}^2 \beta_i^2}{2a_s^2}\right) K_0 \left(\frac{\beta_i R_n}{a_s}\right) I_0 \left(\frac{\beta_i \rho}{a_s}\right). \tag{5}$$

We have found that this function is continuous and that its deviation from $U_{th}^{qu}(\rho; R_n)$ is very small, especially when $\rho \leqslant R_n - a_s$. However, its first derivative is discontinuous at the point $\rho = R_n$.

In the classical calculations, $\rho \leqslant R_n - a_s$, *i.e.*, the discontinuity of $U_{th}^{cl}(\rho; R_n)$, at point $\rho = R_n$, is not included. Therefore, in this case, we use $U_{th}^{cl}(\rho; R_n)$, given by Eqs. (5) and (3), as the needed positron-nanotube interaction potential. On the other hand, we have found that in the quantum mechanical calculations, the discontinuity of $U_{th}^{cl}(\rho; R_n)$, which cannot be excluded, is a source of serious numerical problems. Consequently, in this case, $U_{th}^{qu}(\rho; R_n)$, given by Eqs. (4) and (1)–(3), is required as the needed interaction potential. It should be noted that $U_{th}^{cl}(\rho; R_n)$ and $U_{th}^{qu}(\rho; R_n)$ are cylindrically symmetric.

We would like to emphasize that $U_{th}^{qu}(\rho; R_n)$ represents a circular potential barrier of a finite height, which means that the positron always tunnels through the nanotube wall, *i.e.*, it is always partly dechanneled. However, it has been found that when the nanotube is very short, the positron dechanneling effect is much less pronounced than the channeling effect.

2.2. Classical approach

The vertical and horizontal components of the initial positron position vector, in the impact parameter plane, are denoted as x_0 and y_0, and the vertical and horizontal components of its initial momentum vector as p_{x0} and p_{y0}, respectively. Further, the vertical and horizontal components of the positron position vector during the channeling are denoted as $x(t)$ and $y(t)$, and the vertical and

horizontal components of its momentum vector during the channeling as $p_x(t)$ and $p_y(t)$, respectively, where t denotes time. In the classical calculations, we solve the equations of motion. Since the positron-atom interaction potential is axially averaged, $x(t), y(t), p_x(t)$ and $p_y(t)$ are obtained via the equations of motion in the transverse position plane and the positron-nanotube interaction potential determined by Eqs. (5) and (3). The equations are solved numerically. Since the nanotube is very short, we neglect the positron energy loss and dispersion of its channeling angle. Therefore, the magnitude of the final positron momentum vector, p, is equal to the magnitude of its initial momentum vector, p_0.

In the channeling process under consideration, the critical angle equals $\theta_c = 7.3$ mrad [17]. This means that the angle between the positron momentum vector and nanotube axis is always smaller than θ_c. Therefore, the vertical and horizontal components of the positron channeling angle can be taken to be $\theta_x(t) = p_x(t)/p$ and $\theta_y(t) = p_y(t)/p$, respectively. The initial values of these functions are $\theta_{x0} = p_{x0}/p_0$ and $\theta_{y0} = p_{y0}/p_0$, respectively.

It has been said above that the positron-nanotube interaction potential is cylindrically symmetric. As a result, the mapping of the impact parameter plane to the transverse position plane or the channeling angle plane is reduced to the mapping of, *e.g.*, the x_0 axis in the impact parameter plane to the x axis in the transverse position plane or the θ_x axis in the channeling angle plane. The former mapping, $x(x_0, t)$, will be referred to as the positron spatial channeling function and the latter mapping, $\theta_x(x_0, t)$, as the positron angular channeling function. One can also analyze the diagrams $\tilde{x}(\theta_x, t) = -x[x_0(\theta_x), t]$ and $\tilde{\theta}_x(x, t) = \theta_x[x_0(x), t]$ [17]. The former diagram is the negative inverse of the latter one and vice versa. These diagrams are referred to as the spatial and angular rainbow diagrams of the positrons channeled in the nanotube, respectively.

Let us now introduce the classical spatial and angular Hamilton's principal functions of the positrons channeled in the nanotube, $S_\rho^{cl}(x, t)$ and $S_\theta^{cl}(\theta_x, t)$, respectively. In accordance with a description given in Ref. [26], these functions satisfy the equations

$$\frac{dS_\rho^{cl}(x, t)}{dx} = p\tilde{\theta}_x(x, t) \tag{6}$$

and

$$\frac{dS_\theta^{cl}(\theta_x, t)}{d\theta_x} = p\tilde{x}(\theta_x, t). \tag{7}$$

These equations cannot be solved directly since the functions on their right sides are multi-valued. However, they can be transformed into the equations

$$\frac{d\widetilde{S}_\rho^{cl}(x_0, t)}{dx_0} = p\theta_x(x_0, t)\frac{dx(x_0, t)}{dx_0} \tag{8}$$

and

$$\frac{d\widetilde{S}_\theta^{cl}(x_0, t)}{dx_0} = -px(x_0, t)\frac{d\theta_x(x_0, t)}{dx_0}, \tag{9}$$

respectively, where $\widetilde{S}_\rho^{cl}(x_0, t) = S_\rho^{cl}[x(x_0), t]$ and $\widetilde{S}_\theta^{cl}(x_0, t) = S_\theta^{cl}[\theta_x(x_0), t]$. The functions on the right sides of these equations are single-valued. The equations are solved numerically. Their solutions lead directly to $S_\rho^{cl}(x, t)$ and $S_\theta^{cl}(\theta_x, t)$, respectively.

2.3. Quantum mechanical approach

In the quantum mechanical calculations, the approach is via the time-dependent Schrödinger equation. Since the positron-atom interaction potential is axially averaged, we solve the time-dependent positron Schrödinger equation in the transverse position plane, which is

$$i\hbar\partial_t\psi_s(x, y, t) = -\frac{\hbar^2}{2m}\Delta\psi_s(x, y, t) + U_{qu}^{th}(\rho; R_n)\psi_s(x, y, t), \tag{10}$$

where $\psi_s(x, y, t)$ is the positron wave function in the transverse position plane, $\Delta = \partial^2/\partial x^2 + \partial^2/\partial y^2$, $\partial_t = \partial/\partial t$, m is the positron relativistic mass, and $\hbar$ is the reduced Planck constant.

The initial positron beam is represented as an ensemble of non-interacting Gaussian wave packets [17]. As a result, we implicitly take into account the divergence of the initial beam relative to the nanotube axis. It should be emphasized that such a treatment differs from the previous treatments of positron channeling in crystals [27–29], in which the dynamical diffraction theory was used.

An initial wave packet in the coordinate representation is described by

$$\psi_s(x, y, t = 0; x_0, y_0)$$
$$= \frac{1}{(2\pi)^{1/2}\sigma_\rho}\exp\left[-\frac{(x - x_0)^2 + (y - y_0)^2}{4\sigma_\rho^2}\right], \tag{11}$$

where σ_ρ is its spatial standard deviation. On the other hand, the initial wave packet in the angular representation is defined by

$$\psi_a(\theta_x, \theta_y, t = 0; x_0, y_0) = \frac{1}{(2\pi)^{1/2}\sigma_\theta}\exp\left[-\frac{ip(x_0\theta_x + y_0\theta_y)}{\hbar}\right]$$
$$\times \exp\left(-\frac{\theta_x^2 + \theta_y^2}{4\sigma_\theta^2}\right), \tag{12}$$

which is obtained from the Fourier transform of Eq. (11), where $\sigma_\theta = \Delta_d/(8\ln 2)^{1/2}$ is its angular standard deviation with Δ_d being the initial beam FWHM. Parameters σ_ρ and σ_θ are connected to each other by the corresponding uncertainty principle, resulting in the expression $\sigma_\rho\sigma_\theta = \hbar/(2p)$.

The final wave packet in the coordinate representation is defined by the function $\psi_s(x, y, t; x_0, y_0)$ with $t_f = mL/p$, which is obtained via Eq. (10). The equation is solved numerically [30]. We take that the computation domain is the region $-D_x/2 \leqslant x \leqslant D_x/2$ and $-D_y/2 \leqslant y \leqslant D_y/2$ with $D_x = D_y = 3R_n$. The spatial distribution of transmitted positrons is given as

$$Y_s(x, y) = \sum_{x_0, y_0} c(x_0, y_0)|\psi_s(x, y, t_f; x_0, y_0)|^2, \tag{13}$$

which is a weighted sum of the final positron spatial probability functions over the chosen values of x_0 and y_0, with the pairs of values of x_0 and y_0 chosen within the region $\rho \leqslant R_n - a_s$. This is done as in Ref. [17].

The final wave packet in the angular representation is described by function $\psi_a(\theta_x, \theta_y, t_f; x_0, y_0)$, which is the positron wave function in the channeling angle plane obtained from the Fourier transform of $\psi_s(x, y, t_f; x_0, y_0)$. The transformation is performed numerically. The angular distribution of transmitted positrons is given as

$$Y_a(\theta_x, \theta_y) = \sum_{x_0, y_0} c(x_0, y_0)|\psi_a(\theta_x, \theta_y, t_f; x_0, y_0)|^2, \tag{14}$$

which is the weighted sum of the final positron angular probability functions over the chosen values of x_0 and y_0. It should be noted that $Y_s(x, y)$ and $Y_a(\theta_x, \theta_y)$, which correspond to the whole ensemble of positrons, are cylindrically symmetric.

The exponential form of the function $\psi_s(x, y, t)$ is

$$\psi_s(x, y, t) = A_\rho(x, y, t)\exp[iS_\rho^{qu}(x, y, t)/\hbar], \tag{15}$$

where $A_\rho(x, y, t)$ and $S_\rho^{qu}(x, y, t)/\hbar$ are the amplitude and phase of the function, respectively, determined by its real and imaginary parts. Similarly, the exponential form of the function $\psi_a(\theta_x, \theta_y, t)$ is

$$\psi_a(\theta_x, \theta_y, t) = A_\theta(\theta_x, \theta_y, t) \exp[iS_\theta^{qu}(\theta_x, \theta_y, t)/\hbar], \qquad (16)$$

where $A_\theta(\theta_x, \theta_y, t)$ and $S_\theta^{qu}(\theta_x, \theta_y, t)/\hbar$ are the amplitude and phase of the function, respectively, determined by its real and imaginary parts. In accordance with a consideration contained in Ref. [31], $S_\rho^{qu}(x, y, t)$ and $S_\theta^{qu}(\theta_x, \theta_y, t)$ in fact are the quantum spatial and angular Hamilton's principal functions of a positron channeled in the nanotube, respectively. One should note that these functions, which correspond to one positron from the ensemble, are not cylindrically symmetric.

3. Calculations and discussion

3.1. Classical rainbows

We have calculated and inspected the angular rainbow diagrams of the positrons transmitted through the nanotube, $\tilde{\theta}_x(x, t_f)$, for nanotube lengths $L = 50$–320 nm with a step of 10 nm. Fig. 1 gives the $\tilde{\theta}_x(x, t_f)$ for $L = 320$ nm. The initial positron momentum vector is taken to be parallel to the nanotube axis, *i.e.*, $p_{x0} = p_{y0} = 0$. This curve also represents the associated spatial rainbow diagram, $\tilde{x}(\theta_x, t)$. The positions of the rainbow extrema in the final transverse position (TP) plane are determined by the tangents to the curve perpendicular to the x axis while the positions of the rainbow extrema in the transmission angle (TA) plane are determined by the tangents to it perpendicular to the $\tilde{\theta}_x$ axis [17]. In this case, there are two pairs of extrema in the final TP plane, designated as $\pm 1^s$ and $\pm 2^s$, each of which represents a maximum and minimum of the positron spatial transmission function, $x(x_0, t_f)$, respectively. Hence, there are two circular rainbow lines in the final TP plane. Analysis shows that the positron trajectories that correspond to extrema $\pm 1^s$ involve one deflection from the nanotube wall and the trajectories that correspond to extrema $\pm 2^s$ two deflections from the wall. Consequently, the former extrema is associated with a classical spatial primary rainbow (SPR) and the latter extrema with a classical spatial secondary rainbow (SSR).

Besides, there are two pairs of extrema in the TA plane, designated as $\pm 1^a$ and $\pm 2^a$, each of which represents a maximum and

minimum of the positron angular transmission function, $\theta_x(x_0, t_f)$, respectively. Thus, there are two circular rainbow lines in the TA plane. The former extrema is associated with a classical angular primary rainbow (APR) and the latter extrema with a classical angular secondary rainbow (ASR).

One should observe that the curve in question intersects the $\tilde{\theta}_x$ axis at the origin, a pair of points closer to the origin, $\pm 1^{sa}$, and a pair of points farther from the origin, $\pm 2^{sa}$. Each point from the former pair lies between the points corresponding to the SPR and APR, and each point from the latter pair between the points corresponding to the SSR and ASR. On the other hand, the curve intersects the x axis at the origin and a pair of other points, $\pm 1^{as}$. Each point from the pair lies between the points corresponding to the APR and SSR.

Analysis has shown that in the case under consideration, the angular rainbow diagram of the positrons channeled in the nanotube, $\tilde{\theta}_x(x, t)$, evolves in the following way (see Fig. 1). The initial curve lies on the x axis. Its evolution begins with its left and right branches starting to bend upward and downward, respectively. Then, the curve reaches points $\pm 1^s$, where the evolution direction changes. The former branch continues rightward and upward, and the latter branch leftward and downward. After that, the curve passes through points $\pm 1^{sa}$ and reaches points $\pm 1^a$, where the evolution direction changes again. The former branch continues rightward and downward, and the latter branch leftward and upward. In the further evolution, it passes through points $\pm 1^{as}$, reaches points $\pm 2^s$, passes through points $\pm 2^{sa}$, and reaches points $\pm 2^a$. This means that the sequence of appearance of rainbows in this channeling process is: the SPR, APR, SSR, ASR, *etc.*
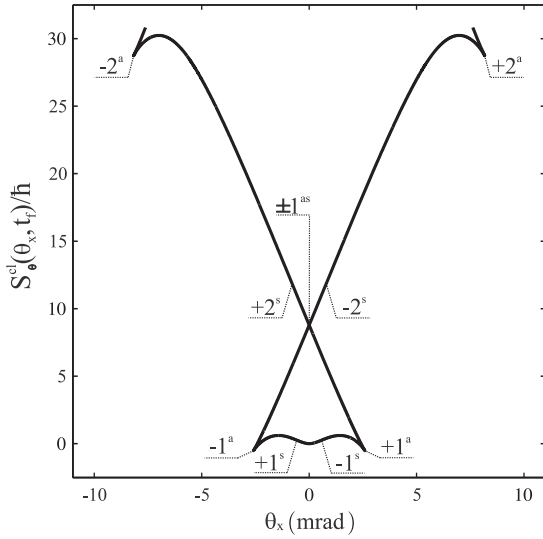
Fig. 2 gives the classical spatial Hamilton's principal function of transmitted positrons for $L = 320$ nm, $S_\rho^{cl}(x, t_f)$, for $p_{x0} = p_{y0} = 0$. The curve representing this function has two pairs of cusp singular
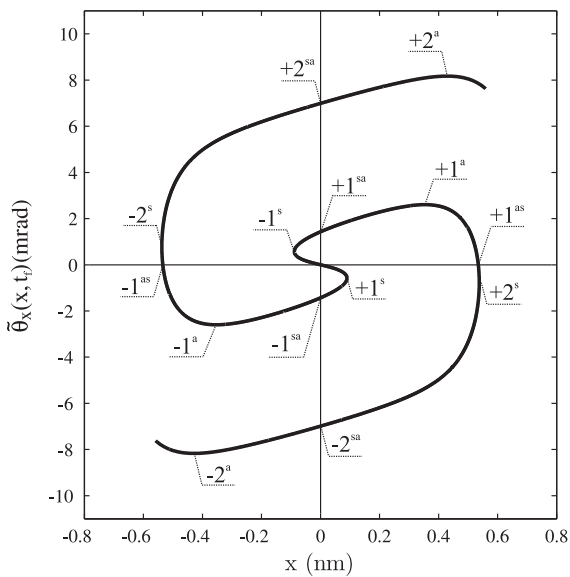
Fig. 1. Angular rainbow diagram of the positrons transmitted through the nanotube of a length of $L = 320$ nm for $p_{x0} = p_{y0} = 0$. Points $\pm 1^s$ and $\pm 2^s$ belong to the classical SPR and SSR, and $\pm 1^a$ and $\pm 2^a$ to the classical APR and ASR, respectively. Points $\pm 1^{sa}$ and $\pm 2^{sa}$ designate the intersections of the curve with the $\tilde{\theta}_x$ axis off the origin and $\pm 1^{as}$ its intersections with the x axis off the origin.
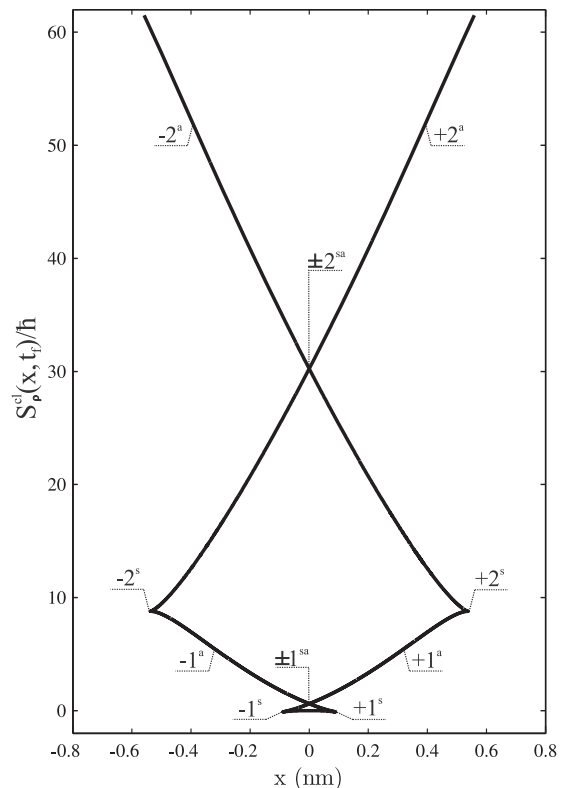
Fig. 2. Classical spatial Hamilton's principal function of transmitted positrons for $L = 320$ nm for $p_{x0} = p_{y0} = 0$ divided by $\hbar$. Points $\pm 1^s$ and $\pm 2^s$ are the cusp singular points of the curve, $\pm 1^a$ and $\pm 2^a$ its inflection points, and $\pm 1^{sa}$ and $\pm 2^{sa}$ its crunode singular points.

Fig. 3. Classical angular Hamilton's principal function of transmitted positrons for $L = 320$ nm for $p_{x0} = p_{y0} = 0$ divided by $\hbar$. Points $\pm 1^a$ and $\pm 2^a$ are the cusp singular points of the curve, $\pm 1^s$ and $\pm 2^s$ its inflection points, and $\pm 1^{as}$ its crunode singular points.

Fig. 4. One-dimensional normalized spatial distribution of the positrons transmitted through the nanotube of a length of $L = 50$ nm described initially as an ensemble of Gaussian wave packets. Maxima $\pm 1^{s0}$ belong to the principal SPR, and maxima $\pm 1^{s1}$, $\pm 1^{s2}$ and $\pm 1^{s3}$ to the supernumerary SPRs.

Fig. 5. Two-dimensional representation of the amplitudes squared of the positron wave functions in the final TP plane along the x axis for $-R_n < x_0 < R_n$ and $y_0 = 0$ in the case of $L = 50$ nm and corresponding positron spatial transmission function. Points $\pm 1^s$ belong to the classical SPR while $\pm 1^{m0}$ designate the maxima of the quantum mechanical distribution. The regions beyond the red lines correspond to the spatial rainbow subensemble. (For interpretation of the references to color in this figure legend, the reader is referred to the web version of this article.)

points, two pairs of inflection points, and two crunode singular points. The cusp singular points closer to the origin correspond to the SPR, $\pm 1^s$, the cusp singular points farther from the origin to the SSR, $\pm 2^s$, the inflection points closer to the origin to the APR, $\pm 1^a$, and the inflection points farther from the origin to the ASR, $\pm 2^a$. The crunode singular points, both lying at the origin, correspond to the two pairs of points where the curve $\tilde{\theta}_x(x, t_f)$ intersects the $\tilde{\theta}_x$ axis off the origin, $\pm 1^{sa}$ and $\pm 2^{sa}$ (see Fig. 1).
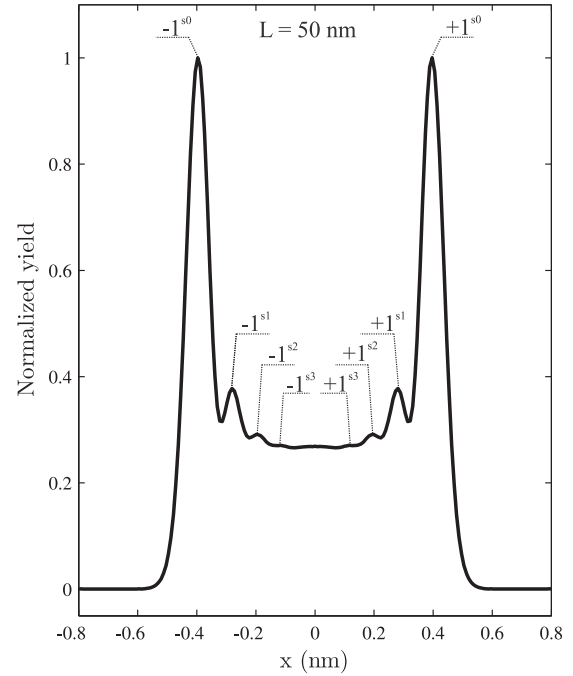
The classical angular Hamilton's principal function of transmitted positrons for $L = 320$ nm, $S_\theta^{cl}(\theta_x, t_f)$, for $p_{x0} = p_{y0} = 0$ is depicted in Fig. 3. The curve representing this function has two pairs of cusp singular points, two pairs of inflection points, and a crunode singular point. The cusp singular points closer to the origin correspond to APR, $\pm 1^a$, the cusp singular points farther from the origin to the ASR, $\pm 2^a$, the inflection points closer to the origin to the SPR, $\pm 1^s$, and the inflection points farther from the origin to the SSR, $\pm 2^s$. The crunode singular point corresponds to the pair of points where curve $\tilde{\theta}_x(x, t_f)$ intersects the x axis off the origin, $\pm 1^{as}$ (see Fig. 1).
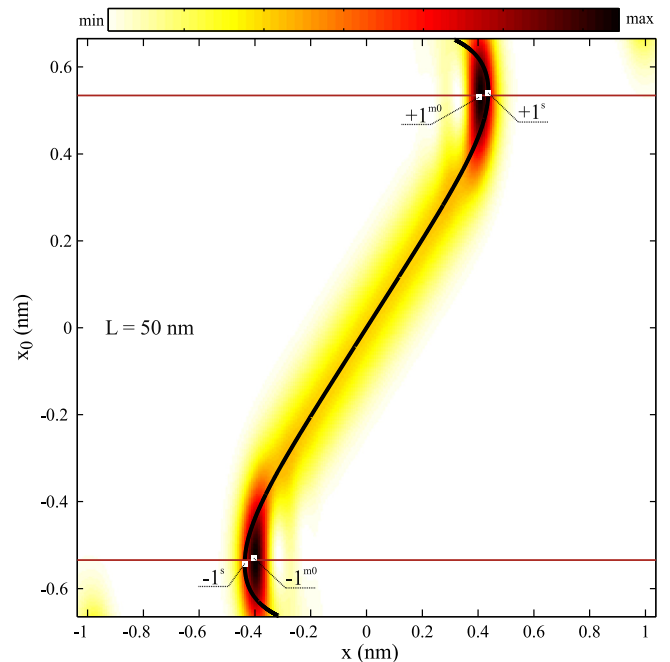
3.2. Quantum rainbows

We are going to present here the cases of transmission of the positrons through the nanotubes of lengths of $L = 50$, 100 and 250 nm. The initial positron beam is assumed to be an ensemble of non-interacting Gaussian wave packets with an angular standard deviation of $\sigma_\theta = 0.1\theta_c = 0.73$ mrad, giving a spatial standard deviation of $\sigma_\rho = 0.19$ nm. The initial number of positrons is $N = 301$. In the cases of $L = 50$ and 100 nm, only the quantum SPR effect is developed, while in the case of $L = 250$ nm, this is true for the SPR, APR and SSR effects. In the case of $L = 250$ nm, we shall describe only the APR effect.

3.2.1. Quantum spatial primary rainbows for $L = 50$ nm
Fig. 4 shows the one-dimensional normalized spatial distribution of transmitted positrons for $L = 50$ nm. It contains a pair of strong maxima at ± 0.40 nm, and three pairs of weaker maxima at ± 0.28 nm, ± 0.20 nm and ± 0.12 nm. Let us explain this distribution.

Fig. 5 gives the positron spatial transmission function, $x(x_0, t_f)$, in the case of $L = 50$ nm. It has a maximum and minimum, $\pm 1^s$, at $x_{01}^s = \pm 0.54$ nm, which are $x_1^s = \pm 0.44$ nm, respectively, belonging to the classical SPR. This means that for x_0 close to x_{01}^s,

the positrons concentrate in the regions just before x_1^s going from the origin. Also, there are no positrons in the regions after x_1^s. Thus, the region before x_1^s is the bright side of the rainbow and the region after x_1^s its dark side. This figure also contains the two-dimensional representation of the amplitudes squared of the positron wave functions in the final TP plane along the x axis, $A_\rho^2(x, y = 0, t_f)$, for $-R_n < x_0 < R_n$ and $y_0 = 0$, *i.e.*, for $\rho_0 = (x_0^2 + y_0^2)^{1/2} < R_n$ and $\varphi_0 = \tan^{-1}(y_0/x_0) = 0$ and π, in the case of $L = 50$ nm. This two-dimensional distribution has a pair of maxima, $\pm 1^{m0}$, at $x_0^{m0} = \pm 0.53$ nm and $x^{m0} = \pm 0.41$ nm, respectively. For x_0 close to zero, these functions have the Gaussian shape with the width larger but close to the initial width. However, for x_0 beyond ± 0.26 nm going from the origin, each of these functions has a few clearly observable maxima or shoulders – it is wrinkled. This is to be attributed to the effect of internal focusing of the corresponding wave packet. Namely, a ray within the wave packet entering the nanotube at a smaller distance from its wall then the neighboring ray can exit the nanotube at a point very close to the final point of the neighboring ray. Hence, a few focal points appear on the x axis, where the neighboring rays of the wave packet come very close to each other (in the TP plane). The effect is analogous to the one described by Born and Wolf [32]. The positions of the observed maxima or shoulders coincide with the positions of these internal focal points.

It should be emphasized that this explanation of the effect of wave wrinkling is more general than the one given by Petrović et al. [17]. It applies for all the values of x_0 for which the effect occurs while the previous explanation is restricted to the ones close to x_0^{m0}.

The positions of the maxima or shoulders of one of the functions $A_\rho^2(x, y = 0, t_f)$ are close to the positions of the corresponding maxima or shoulders of the other functions. Hence, one can say that the wave packets wrinkle in a mutually coordinated way. We explain this by the fact that all the projectiles interact with the same target. For x_0 close to x_0^{m0}, each function contains a pronounced maximum close to x^{m0}. The corresponding wave packet is wrinkled as if a barrier exists at x^{m0}, preventing its spreading after the barrier, and, hence, causing its concentration just before the barrier. It is also evident that the curve connecting the positions of the absolute maxima of $A_\rho^2(x, y = 0, t_f)$ is close to the curve representing the function $x(x_0, t_f)$. Therefore, we conclude that the above described effects of wave wrinkling, coordination and concentration make a quantum SPR effect. The observed virtual barrier represents the boundary between the bright and dark sides of the rainbow.

Fig. 6 gives the one-dimensional representation of the functions $A_\rho^2(x, y = 0, t_f)$ for $-R_n < x_0 < R_n$ and $y_0 = 0$ in the case of $L = 50$ nm. In order to make the figure clearer, the number of curves is reduced from $N = 301$ to 61. One can see that each of these curves that is centered farther from the origin (for x_0 beyond ± 0.26 nm) is wrinkled. The curves designated by red color correspond to the wave packets belonging to a spatial rainbow subensemble that will be specified later.

Fig. 7(a) gives the two-dimensional initial spatial distribution of a positron assumed to be a Gaussian wave packet placed at point (+0.53 nm, 0), where the distribution $A_\rho^2(x, y = 0, t_f)$ is maximal. The resulting spatial distribution of the wave packet transmitted through the nanotube of a length of $L = 50$ nm is given in Fig. 7 (b). It contains a strong maximum and a number of weaker maxima extending toward the nanotube axis – it is wrinkled.

Fig. 8 shows the classical spatial Hamilton's principal function of the positrons transmitted through the nanotube divided by $\hbar$, $S_\rho^{cl}(x, t_f)/\hbar$, in the case of $L = 50$ nm. The curve representing this
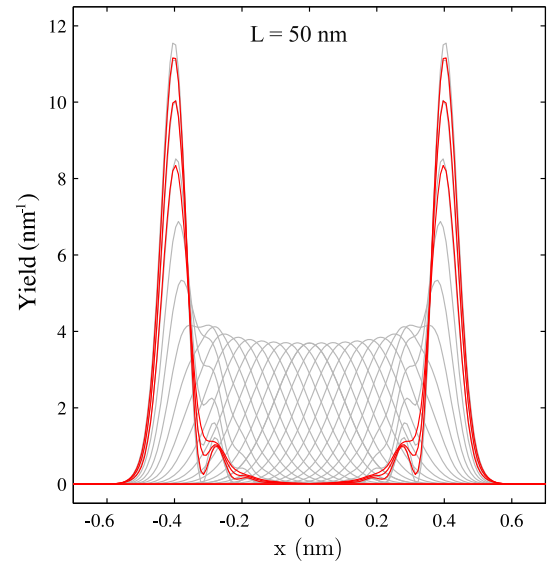

Fig. 6. One-dimensional representation of the amplitudes squared of the positron wave functions in the final TP plane along the x axis for $-R_n < x_0 < R_n$ and $y_0 = 0$ in the case of $L = 50$ nm. The curves designated by red color correspond to the spatial rainbow subensemble. (For interpretation of the references to color in this figure legend, the reader is referred to the web version of this article.)

function has a pair of cusp singular points, $\pm 1^s$, at $x_1^s = \pm 0.44$ nm, corresponding to the maximum and minimum of the function $x(x_0, t_f)$, respectively. It has three branches, joining at the cusp singular points, which will be referred to as its horizontal branch, and its right and left vertical branches.

Fig. 8 also gives the phases of the positron wave functions in the final TP plane along the x axis, $S_\rho^{qu}(x, y = 0, t_f)/\hbar$, for $-R_n < x_0 < R_n$ and $y_0 = 0$ in the case of $L = 50$ nm. The number of curves is 61, instead of $N = 301$. It is evident that there are several groups of curves representing these functions. The curves from each of these groups extend together with the remaining curves in the directions from the right nanotube wall, at $+R_n = +0.69$ nm, to the right cusp singular point, $+1^s$, and from the left wall, at $-R_n = -0.69$ mm, to the left singular point, -1^s, and then separate from the remaining curves and continue "parallel" to the right and left vertical branches of the curve representing the function $S_\rho^{cl}(x, t_f)/\hbar$, respectively. Let us focus on the curves from the first group, which are most numerous and separate first. They are designated by red color. The percentage of curves from this group is 19.3% and the corresponding values of x_0 are beyond $x_0^{r0} = \pm 0.54$ nm going from the origin (see Fig. 5). There are 21 additional groups of curves. The percentages of curves from these groups are close to each other as well as the corresponding intervals of values of x_0, extending from x_0^{r0} toward the origin. The average percentage of curves from these groups is 3.8% while the corresponding average interval of values of x_0 is 0.03 nm. If the number of shown curves were not reduced, the figure would contain more curves from these groups.
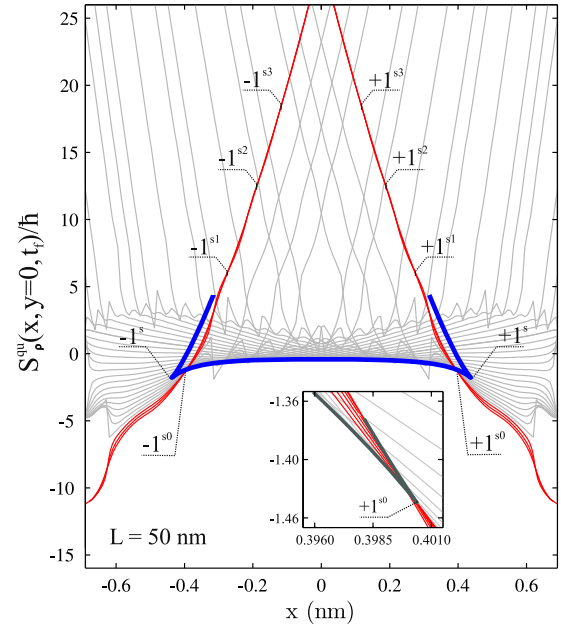
The curves from the right or left subgroup of the first group are close to each other, meaning that the corresponding wave packets are close to being in phase with each other. This means that the behavior of these wave packets is additionally coordinated. Besides, these curves are close to the right or left vertical branch. A detailed analysis of all the curves in the regions around the former cusp singular points, $\pm 1^s$, has shown that their envelope also has a pair of cusp singular points, $\pm 1^{s0}$, at $x_1^{s0} = \pm 0.40$ nm, which are close to x^{m0} (see Fig. 5). The "vertical" branches of the right and left parts of the envelope are defined by the curves from the
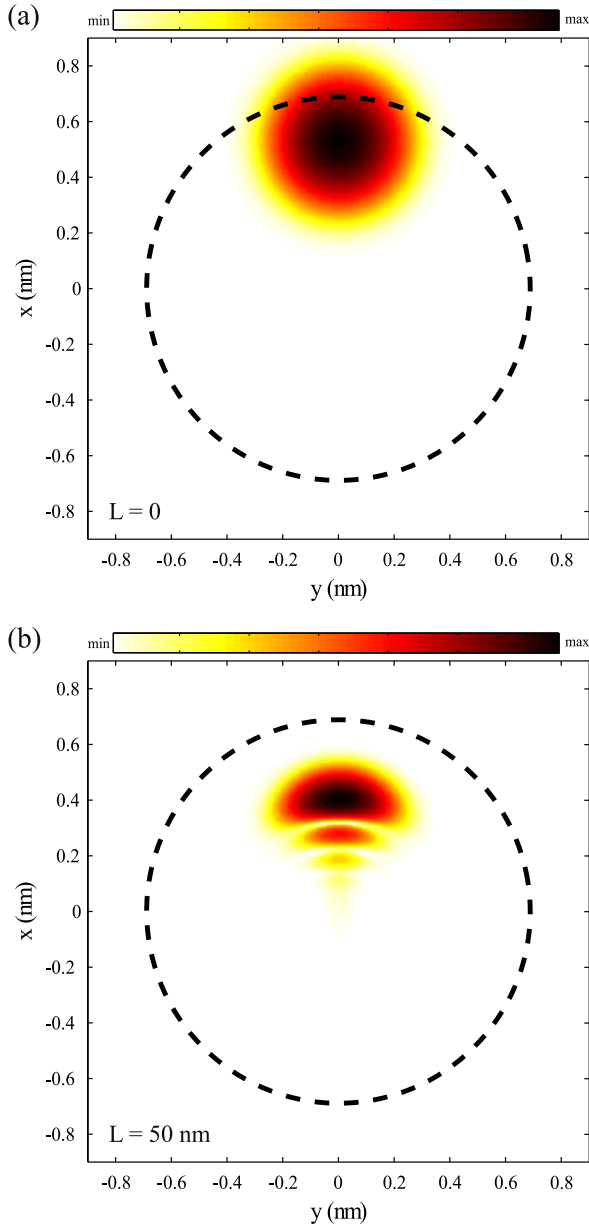
Fig. 7. (a) Two-dimensional initial spatial distribution of a positron described as a Gaussian wave packet placed at point (+0.53 nm, 0), and (b) resulting spatial distribution of the positron transmitted through the nanotube of a length of =50 nm graphed on a logarithmic scale.

Fig. 8. Phases of the positron wave functions in the final TP plane along the x axis for $-R_n < x_0 < R_n$ and $y_0 = 0$ in the case of $L = 50$ nm – the gray and red curves, and corresponding classical spatial Hamilton's principal function divided by $\hbar$ – the blue curve. The curves designated by red color correspond to the spatial rainbow subensemble. Points $\pm 1^s$ are the cusp singular points of the classical curve. Points $\pm 1^{s0}$ are the cusp singular points of the envelopes of the quantum mechanical curves in the region around $\pm 1^s$, and $\pm 1^{s1}$, $\pm 1^{s2}$ and $\pm 1^{s3}$ are the common inflection points of these curves that correspond to the rainbow subensemble. Inset: the envelope of the quantum mechanical curves in the region around $+1^s$ – the green curve, with singular point $+1^{s0}$. (For interpretation of the references to color in this figure legend, the reader is referred to the web version of this article.)

right and left subgroups of the first group, respectively, and its "horizontal" branch by the remaining curves. This is shown in the inset of Fig. 8 for the singular point $+1^{s0}$. Thus, the latter singular points are the points of separation of the curves from the first group from the remaining curves. A careful inspection of the curves from the right and left subgroups of the first group after the separation points has shown that each of them has three inflection points, and that the positions of these points coincide with the positions of the corresponding inflection points of the other curves from the subgroup. The positions of these three pairs of common inflection points are $x_1^{s1} = \pm 0.27$ nm, $x_1^{s2} = \pm 0.18$ nm and $x_1^{s3} = \pm 0.10$ nm.

The same analyses have been performed for the wave packets with $\rho_0 < R_n$ and the other values of φ_0, different from 0 and π. Its conclusions coincide with those drawn from the analysis for

$\varphi_0 = 0$ and π, with the values of $x_1^{s0}, x_1^{s1}, x_1^{s2}$ and x_1^{s3} coinciding or being close to the ones obtained for $\varphi_0 = 0$ and π.

Now, we can come back to the one-dimensional normalized spatial distribution of transmitted positrons for $L = 50$ nm, given in Fig. 4. The positions of the strong maxima coincide with $\pm x_1^{s0}$, and the positions of the weaker maxima are close to x_1^{s1}, x_1^{s2} and x_1^{s3}. They are denoted as $\pm 1^{s0}, \pm 1^{s1}, \pm 1^{s2}$ and $\pm 1^{s3}$, respectively. The small differences between the positions of the weaker maxima and x_1^{s1}, x_1^{s2} and x_1^{s3}, respectively, are attributed to the fact that the distribution is generated with all the values of x_0 and y_0, rather that with only the values x_0 beyond x_0^{r0} and $y_0 = 0$. The strong maxima belong to a principal SPR and the weaker maxima to three supernumerary SPRs. The positions of the stronger maxima are the common positions of the points of separation of all the wave packets from the first group. The positions of the weaker maxima are determined dominantly by the common positions of the inflection points of the phases of all the wave packets from the first group. The subensemble comprising the wave packets from the first group has been named the spatial rainbow subensemble.

3.2.2. Quantum spatial primary rainbows for L = 100 nm

Fig. 9 shows the one-dimensional normalized spatial distribution of transmitted positrons for $L = 100$ nm. It contains a pair of weaker maxima at ± 0.23 nm and a stronger maximum at the origin. The explanation of this distribution is the same as the one already given for the distribution obtained for $L = 50$ nm.
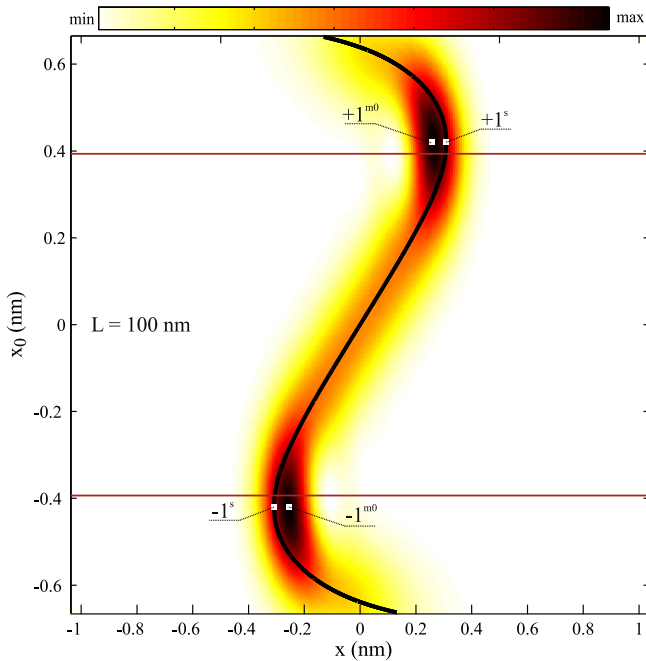
Fig. 10 gives the function $x(x_0, t_f)$ in the case of $L = 100$ nm. It has a maximum and minimum, $\pm 1^s$, at $x_{01}^s = \pm 0.42$ nm, which are $x_1^s = \pm 0.31$ nm, respectively, belong to the classical SPR. This figure also contains the functions $A_\rho^2(x, y = 0, t_f)$ for $-R_n < x_0 < R_n$ and $y_0 = 0$ in the case of $L = 100$ nm. This two-dimensional
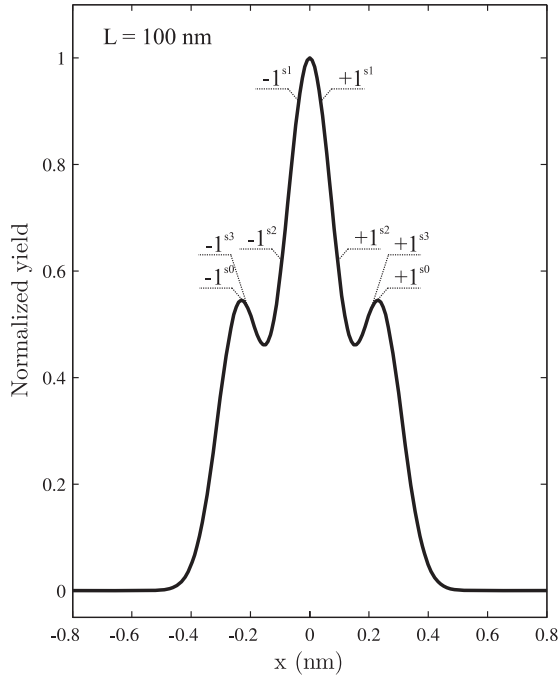
Fig. 9. One-dimensional normalized spatial distribution of the positrons transmitted through the nanotube of a length of $L = 100$ nm represented initially as an ensemble of Gaussian wave packets. The weaker maxima are due to the principal SPR combined with the third supernumerary SPR, $\pm 1^{s0}$ and $\pm 1^{s3}$, and the stronger maximum is due to the first and second supernumerary SPRs, $\pm 1^{s1}$ and $\pm 1^{s2}$, respectively.
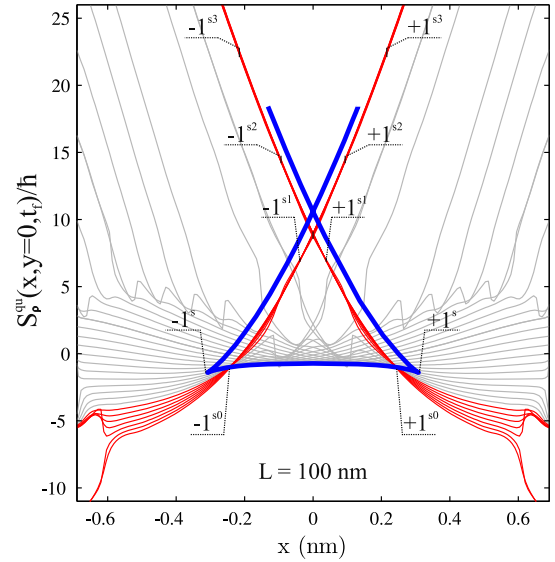
Fig. 11. Phases of the positron wave functions in the final TP plane along the x axis for $-R_n < x_0 < R_n$ and $y_0 = 0$ in the case of $L = 100$ nm – the gray and red curves, and corresponding classical spatial Hamilton's principal function divided by $\hbar$ – the blue curve. The curves designated by red color correspond to the spatial rainbow subensemble. Points $\pm 1^s$ are the cusp singular points of the classical curve. Points $\pm 1^{s0}$ are the cusp singular points of the envelopes of the quantum mechanical curves in the region around $\pm 1^s$, and $\pm 1^{s1}$, $\pm 1^{s2}$ and $\pm 1^{s3}$ are the common inflection points of these curves that correspond to the rainbow subensemble. (For interpretation of the references to color in this figure legend, the reader is referred to the web version of this article.)

Fig. 10. Two-dimensional representation of the amplitudes squared of the positron wave functions in the final TP plane along the x axis for $-R_n < x_0 < R_n$ and $y_0 = 0$ in the case of $L = 100$ nm and corresponding positron spatial transmission function. Points $\pm 1^s$ belong to the classical SPR while $\pm 1^{m0}$ designate the maxima of the quantum mechanical distribution. The regions beyond the red lines correspond to the spatial rainbow subensemble. (For interpretation of the references to color in this figure legend, the reader is referred to the web version of this article.)

distribution has a pair of maxima, $\pm 1^{m0}$, at $x_0^{m0} = \pm 0.42$ nm and $x^{m0} = \pm 0.26$ nm. Analysis has shown that the above described effects of wave wrinkling, coordination and concentrate appear

in this case as well, and that they make a quantum SPR effect. The observed virtual barrier, at x^{m0}, is the boundary between the bright and dark sides of the rainbow.

Fig. 11 shows the function $S_\rho^{cl}(x, t_f)/\hbar$ in the case of $L = 100$ nm. The curve representing this function has a pair of cusp singular points, $\pm 1^s$, at $x_1^s = \pm 0.31$ nm, and one crunode singular point, at the origin ($\pm 1^{sa}$). The cusp singular points correspond to the maximum and minimum of the function $x(x_0, t_f)$, respectively, and the crunode singular point corresponds to a pair of points where the curve representing the function $\tilde{\theta}_x(x, t_f)$ intersects the $\tilde{\theta}_x$ axis off the origin (see Fig. 1).

Fig. 11 also gives the functions $S_\rho^{qu}(x, y = 0, t_f)/\hbar$ for $-R_n < x_0 < R_n$ and $y_0 = 0$ in the case of $L = 100$ nm. The number of curves is 61, instead of $N = 301$. The curves representing these functions that belong to the first group, *i.e.*, that correspond to the wave packets from the spatial rainbow subensemble are designated by red color. The values of x_0 in question are beyond $x_0^{r0} = \pm 0.39$ nm going from the origin (see Fig. 10). The envelope of all the curves in the regions around the former cusp singular points, $\pm 1^s$, also has a pair of cusp singular points, $\pm 1^{s0}$, at $x_1^{s0} = \pm 0.26$ nm, coinciding with x^{m0} (see Fig. 10). These are the points of separation of the curves from the first group from the remaining curves. Each of the curves from the right and left subgroup of the first group has three inflection points after the separation point. The positions of the three pairs of common inflection points of these curves are $x_1^{s1} = \pm 0.04$ nm, $x_1^{s2} = \mp 0.09$ nm and $x_1^{s3} = \mp 0.22$ nm. The values of $x_1^{s0}, x_1^{s1}, x_1^{s2}$ and x_1^{s3} obtained for the wave packets with $\rho_0 < R_n$ and the other values of φ_0, different from 0 and π, coincide or are close to the ones obtained for $\varphi_0 = 0$ and π.

Comparison of the positions of the maxima of the one-dimensional normalized spatial distribution of transmitted positrons for $L = 100$ nm, given in Fig. 9, with $x_1^{s0}, x_1^{s1}, x_1^{s2}$ and x_1^{s3} leads

to the conclusion that the weaker maxima are to be attributed to the principal SPR combined with the third supernumerary SPR, $\pm1^{s0}$ and $\pm1^{s3}$, and that the stronger maximum is to be attributed to the first and second supernumerary SPRs, $\pm1^{s1}$ and $\pm1^{s2}$, respectively.

3.2.3. Quantum angular primary rainbows for L = 250 nm

Fig. 12 shows the one-dimensional normalized angular distribution of transmitted positrons for $L = 250$ nm. One can view it as a superposition of a strong bell-shaped component centered at the origin, and a component consisting of two pairs of maxima at ±2.3 mrad and ±1.0 mrad, with the second pair of maxima seen in the distribution as a pair of shoulders. We shall explain this distribution in a way analogous to the one already given for the distributions obtained for $L = 50$ and 100 nm.

Fig. 13 gives the positron angular transmission function, $\theta_x(x_0, t_f)$, in the case of $L = 250$ nm. It has a maximum and minimum, $\pm1^a$, at $x_{01}^a = \mp0.54$ nm, which are $\theta_{x1}^a = \pm3.8$ mrad, respectively, belonging to the classical APR. This means that for x_0 close to x_{01}^a, the positrons concentrate in the regions just before θ_{x1}^a going from the origin. Also, there are no positrons in the regions after θ_{x1}^a. Thus, the region before θ_{x1}^a is the bright side of the rainbow and the region after θ_{x1}^a its dark side. This figure also contains the two-dimensional representation of the amplitudes squared of the positron wave functions in the TA plane along the θ_x axis, $A_\theta^2(\theta_x, \theta_y = 0, t_f)$, for $-R_n < x_0 < R_n$ and $y_0 = 0$ in the case of $L = 250$ nm. This two-dimensional distribution has two pairs of maxima, $\pm1^{m0}$ and $\pm1^{m1}$, at $x_0^{m0} = \mp0.46$ nm and $\theta_x^{m0} = \pm2.8$ mrad, and $x_0^{m1} = \mp0.11$ nm and $\theta_x^{m1} = \pm0.5$ mrad, respectively. For x_0 close to zero, these functions have the Gaussian shape with the width smaller but close to the initial width. However, for x_0 beyond ±0.33 nm going from the origin, each of these functions has a few clearly observable maxima or shoulders – it is wrinkled. This is to be attributed to the effect of internal focusing of the corresponding
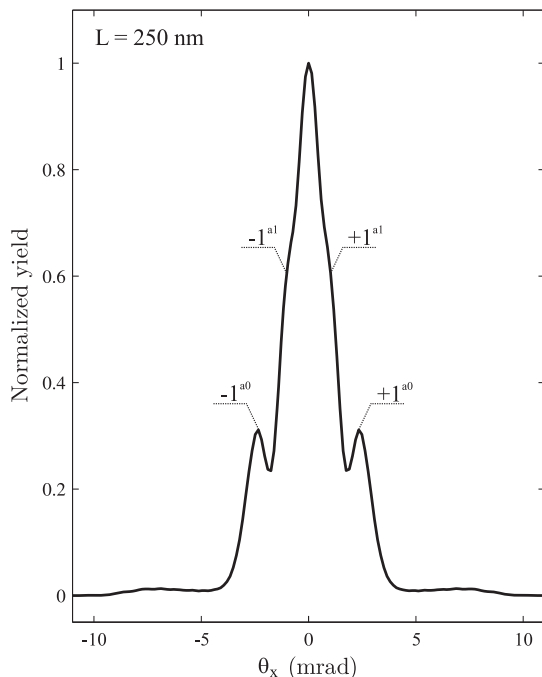

Fig. 13. Two-dimensional representation of the amplitudes squared of the positron wave functions in the TA plane along the θ_x axis for $-R_n < x_0 < R_n$ and $y_0 = 0$ in the case of $L = 250$ nm and corresponding positron angular transmission function. Points $\pm1^a$ belong to the classical APR, while $\pm1^{m0}$ and $\pm1^{m1}$ designate the maxima of the quantum mechanical distribution. The regions beyond the red lines correspond to the angular rainbow subensemble. (For interpretation of the references to color in this figure legend, the reader is referred to the web version of this article.)

wave packet. Namely, a ray within the wave packet entering the nanotube at a larger angle relative to its wall than the neighboring ray can exit the nanotube at an angle very close to the final angle of the neighboring ray. Hence, a few focal points appear on the θ_x axis, where the neighboring rays of the wave packet come very close to each other (in the TA plane) [32]. The positions of the observed maxima or shoulders coincide with the positions of these internal focal points.

The positions of the maxima or shoulders of one of the functions $A_\theta^2(\theta_x, \theta_y = 0, t_f)$ are close to the positions of the corresponding maxima or shoulders of the other functions. This means that the wave packets wrinkle in a mutually coordinated way. For x_0 close to x_0^{m0}, each function contains a pronounced maximum at θ_x^{m0}. The corresponding wave packet is wrinkled as if a barrier exists at θ_x^{m0}, causing its concentration just before the barrier. One can also see that the curve connecting the positions of the absolute maxima of $A_\theta^2(\theta_x, \theta_y = 0, t_f)$ is close to the curve representing the function $\theta_x(x_0, t_f)$. Thus, the conclusion is that the above described effects of wave wrinkling, coordination and concentration make a quantum APR effect. The observed virtual barrier represents the boundary between the bright and dark sides of the rainbow.

Fig. 14(a) gives the two-dimensional initial angular distribution of a positron assumed to be a Gaussian wave packet placed at point $(+0.46$ mrad, 0$)$, where the distribution $A_\theta^2(\theta_x, \theta_y = 0, t_f)$ is maximal. The resulting angular distribution of the wave packet transmitted through the nanotube of a length of $L = 250$ nm is given in Fig. 14(b). It contains a strong maximum and a number of weaker maxima extending toward the origin and beyond – it is wrinkled.

Fig. 15 shows the classical angular Hamilton's principal function of the positrons transmitted through the nanotube divided by $\hbar$, $S_\theta^{cl}(\theta_x, t_f)/\hbar$, in the case of $L = 250$ nm. The curve representing this function has a pair of cusp singular points, $\pm1^a$, at $\theta_{x1}^a = \pm3.8$ nm, and one crunode singular point, at the origin $(\pm1^{as})$. The cusp

Fig. 12. One-dimensional normalized angular distribution of the positrons transmitted through the nanotube of a length of $L = 250$ nm represented initially as an ensemble of Gaussian wave packets. Maxima $\pm1^{a0}$ belong to the principal APR and shoulders $\pm1^{a1}$ to the first supernumerary APR.
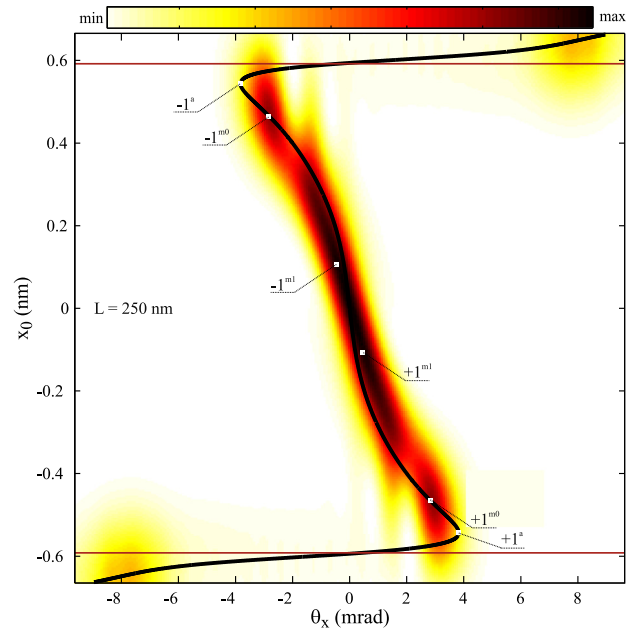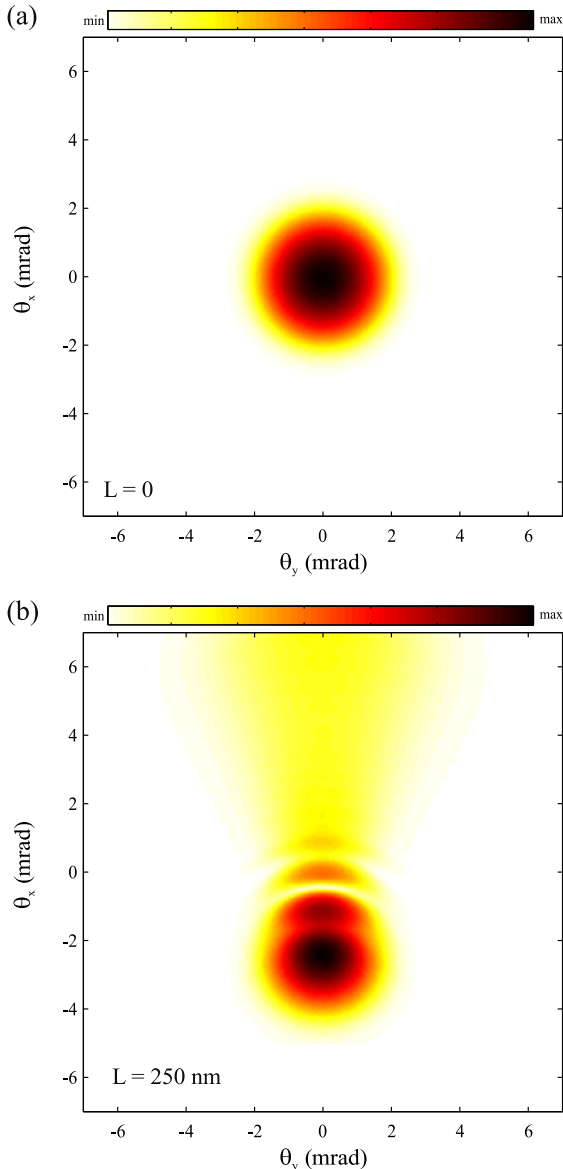
singular points correspond to the maximum and minimum of the function $\theta_x(x_0, t_f)$, respectively, and the crunode singular point corresponds to a pair of points where the curve representing the function $\tilde{\theta}_x(x, t_f)$ intersects the x axis off the origin (see Fig. 1). The curve representing $S_\theta^{cl}(\theta_x, t_f)/\hbar$ has three branches, joining at the cusp singular points, which will be referred to as its horizontal branch, and its right and left vertical branches.

Fig. 15 also gives the phases of the positron wave functions in the TA plane along the θ_x axis, $S_\theta^{qu}(\theta_x, \theta_y = 0, t_f)/\hbar$, for $-R_n < x_0 < R_n$ and $y_0 = 0$ in the case of $L = 250$ nm. The number of curves is 61, instead of $N = 301$. One can see that there are several groups of curves representing these functions. The curves from each of these groups extend together with the remaining curves in the directions from the right limit, determined by $+\theta_c = +7.3$ mrad, to the right cusp singular point, $+1^a$, and from the left limit, determined by $-\theta_c = -7.3$ mrad, to the left singular point, -1^a, and then separate from the remaining curves and
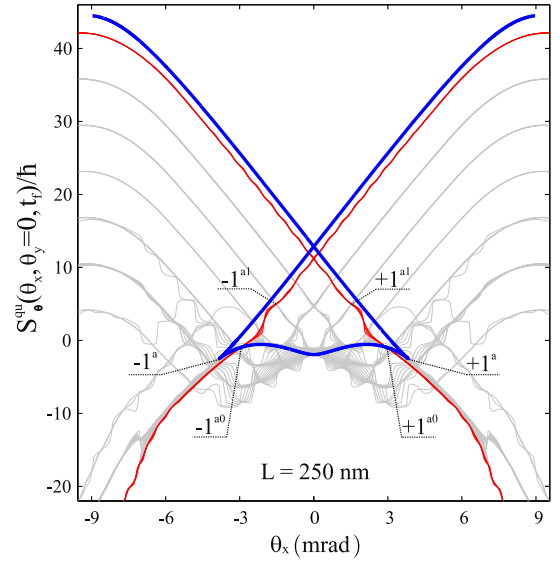
Fig. 15. Phases of the positron wave functions in the TA plane along the θ_x axis for $-R_n < x_0 < R_n$ and $y_0 = 0$ in the case of $L = 250$ nm – the gray and red curves, and corresponding classical angular Hamilton's principal function divided by $\hbar$ – the blue curve. The curves designated by red color correspond to the angular rainbow subensemble. Points $\pm 1^a$ are the cusp singular points of the classical curve. Points $\pm 1^{a0}$ are the cusp singular points of the envelopes of the quantum mechanical curves in the region around $\pm 1^a$, and $\pm 1^{a1}$ are the common inflection points of these curves that correspond to the rainbow subensemble. (For interpretation of the references to color in this figure legend, the reader is referred to the web version of this article.)

continue "parallel" to the right and left vertical branches of the curve representing the function $S_\theta^{cl}(\theta_x, t_f)/\hbar$, respectively. We shall focus on the curves from the first group, which separate first. They are designated by red color. The corresponding values of x_0 are beyond $x_0^{r0} = \pm 0.59$ nm going from the origin (see Fig. 13). The subensemble comprising the wave packets from the first group is called the angular rainbow subensemble.

The curves from the right or left subgroup of the first group are close to each other, meaning that the corresponding wave packets are close to being in phase with each other. This means that the behavior of these wave packets is additionally coordinated. Besides, these curves are close to the right or left vertical branch. A detailed analysis of all these curves in the regions around the former cusp singular points, $\pm 1^a$, has shown that their envelope also has a pair of cusp singular points, $\pm 1^{a0}$, at $\theta_{x1}^{a0} = \pm 3.00$ nm, being close to $\pm \theta_x^{m0}$ (see Fig. 13). The "vertical" branches of the right and left envelopes are defined by the curves from the right and left subgroups of the first group, respectively, and their "horizontal" branches by the remaining curves. This means that the latter singular points are the points of separation of the curves from the first group from the remaining curves. A careful inspection of the curves from the right and left subgroups of the first group after the separation point shows that each of them has several inflection points, and that the positions of these points coincide with the positions of the corresponding inflection points of the other curves from the subgroup. We shall take into account here only the right and left inflection points that lie next to the latter singular points. The positions of the corresponding pair of common inflection points are $\theta_{x1}^{a1} = \pm 1.5$ mrad. The values of θ_{x1}^{a0} and θ_{x1}^{a1} obtained for the wave packets with $\rho_0 < R_n$ and the other values of φ_0, different from 0 and π, coincide or are close to the ones obtained for $\varphi_0 = 0$ and π.

We can now come back to the one-dimensional normalized angular distribution of transmitted positrons for $L = 250$ nm, given in Fig. 12. Its strong bell-shaped component corresponds to the maximum of the distribution $A_\theta^2(\theta_x, \theta_y = 0, t_f)$ at x_0^{m1} and $\theta_x^{m1}, \pm 1^{m1}$

Fig. 14. (a) Two-dimensional initial angular distribution of a positron described as a Gaussian wave packet placed at point (+0.46 nm, 0), and (b) resulting angular distribution of the positron transmitted through the nanotube of a length of $L = 250$ nm graphed on a logarithmic scale.

(see Fig. 13). Since the positions of the maxima and shoulders of the distribution are close to θ_{x1}^{a0} and θ_{x1}^{a1}, they are denoted as $\pm 1^{a0}$ and $\pm 1^{a1}$, respectively. The small differences between the positions of the maxima and shoulders and θ_{x1}^{a0} and θ_{x1}^{a1}, respectively, are attributed to the fact that the distribution is generated with all the values of x_0 and y_0, rather then with only the values x_0 beyond x_0^{r0} and $y_0 = 0$. The maxima belong to a principal APR and the shoulders to a supernumerary APR. The positions of the maxima are the common positions of the points of separation of all the wave packets from the angular rainbow subensemble. The positions of the shoulders are determined dominantly by the common positions of the chosen inflection points of the phases of all the wave packets from the angular rainbow subensemble. It has been found that the other inflection points of the phases of the wave packets from the angular rainbow subensemble are connected to the weak supernumerary APRs, and to the principal and supernumerary ASRs, not being well-developed. The maxima of the distribution corresponding to the ASRs, lying in the regions after about ± 5 mrad going from the origin, can be seen in the figure.

4. Conclusions

In the classical part of the study, we have analyzed the angular rainbow diagram of the positrons transmitted through the nanotube of a length of $L = 320$ nm for $p_{x0} = p_{y0} = 0$, and demonstrated that in this case, a SPR, APR, SSR and ASR occur. The corresponding classical spatial and angular Hamilton's principal functions have been presented as well.

In the quantum mechanical part of the study, we have shown and explained in detail the spatial distributions of the positrons transmitted through the nanotubes of lengths of $L = 50$ and 100 nm. The initial positron beam has been represented as an ensemble of non-interacting Gaussian wave packets. Analysis of the amplitudes squared of the positron wave functions in the final TP plane for different values of the components of the initial positron position vector has demonstrated that each of these functions has a few maxima or shoulders, *i.e.*, it is wrinkled. This is attributed to the appearance of a few focal points on the observation axis in the final TP plane, where the neighboring rays of the wave packet come very close to each other. Besides, we have found that the wave packets wrinkle in a mutually coordinated way. This has been explained by the fact that all the projectiles interact with the same target. In addition, each wave packet is wrinkled as if a barrier exists at a certain point on the observation axis, preventing its spreading after the barrier, and, hence, causing its concentration just before the barrier. The conclusion has been that the effects of wave wrinkling, coordination and concentration make a quantum SPR effect. The observed virtual barrier represents the boundary between the bright and dark sides of the rainbow.

We have also explored in detail the phases of the positron wave functions in the final TP plane for different values of the components of the initial positron position vector in the cases of $L = 50$ and 100 nm. It has been found that the envelopes of the curves representing these functions have the cusp singular points, and that these points determine the position of the principal SPR. Besides, the curves representing these functions have the common inflection points, which determine the positions of the supernumerary SPR.

The quantum mechanical part of the study has also included a detailed investigation of the angular distribution of the positrons transmitted through the nanotubes of a length of $L = 250$ nm. Again, the initial positron beam has been represented as an ensemble of non-interacting Gaussian wave packets. The analysis has been performed in a way analogous to the one applied in the considerations of the spatial distributions of transmitted positrons. As in these considerations, we have observed the effects of wave wrinkling, coordination and concentration, and concluded that they make a quantum APR effect.

References

[1] M.T. Robinson, O.S. Oen, Phys. Rev. 132 (1963) 2385.
[2] J. Lindhard, Mat. Fys. Medd. Dan. Vid. Selsk 34 (1965) 1.
[3] D.S. Gemmell, Rev. Mod. Phys. 46 (1974) 129.
[4] N. Nešković, Phys. Rev. B 33 (1986) 6030.
[5] H.F. Krause, S. Datz, P.F. Dittner, J. Gomez del Campo, P.D. Miller, C.D. Moak, N. Nešković, P.L. Pepmiller, Phys. Rev. B 33 (1986) 6036.
[6] S. Petrović, L. Miletić, N. Nešković, Phys. Rev. B 61 (2000) 184.
[7] M. Motapothula, S. Petrović, N. Nešković, Z.Y. Dang, M.B.H. Breese, M.A. Rana, A. Osman, Phys. Rev. B 86 (2012) 205426.
[8] S. Petrović, N. Nešković, M. Ćosić, M. Motapothula, M.B.H. Breese, Nucl. Instr. Meth. Phys. Res. B 360 (2015) 23.
[9] S. Iijima, Nature 354 (1991) 56.
[10] R. Saito, G. Dresselhaus, M.S. Dresselhaus, The Physical Properties of Carbon Nanotubes, Imperial College Press, 1998.
[11] R.H. Baughman, A.A. Zakhidov, W.A. de Heer, Science 297 (2002) 787.
[12] V.V. Klimov, V.S. Letokhov, Phys. Lett. A 222 (1996) 424.
[13] D. Borka, S. Petrović, N. Nešković, Channeling of Protons through Carbon Nanotubes, Nova Science Publishers, New York, 2011.
[14] S. Petrović, D. Borka, N. Nešković, Eur. Phys. J. B 44 (2005) 41.
[15] D. Borka, S. Petrović, N. Nešković, D.J. Mowbray, Z.L. Mišković, Phys. Rev. A 73 (2006) 062902.
[16] S. Petrović, I. Telečki, D. Borka, N. Nešković, Phys. Lett. A 372 (2008) 6003.
[17] S. Petrović, M. Ćosić, N. Nešković, Phys. Rev. A 88 (2013) 012902.
[18] Z. Zhu, D. Zhu, R. Lu, Z. Xu, W. Zhang, H. Xia, in: S.B. Dabagov (Ed.), International Conference on Charged and Neutral Particles Channeling Phenomena, vol. 5974, SPIE, Bellingham, Washington, 2005, pp. 597413-1–597413-8.
[19] G. Chai, H. Heinrich, L. Chow, T. Schenkel, Appl. Phys. Lett. 91 (2007) 103101.
[20] M. Ćosić, S. Petrović, N. Nešković, Nucl. Instr. Meth. Phys. Res. Sect. B 323 (2014) 30.
[21] G. Molière, Z. Naturforsch 2a (1947) 133.
[22] X. Artru, S.P. Fomin, N.F. Shul'ga, K.A. Ispirian, N.K. Zhevago, Phys. Rep. 412 (2005) 89.
[23] H.F. Krause, J.H. Barrett, S. Datz, P.F. Dittner, N.L. Jones, J. Gomez del Campo, C. R. Vane, Phys. Rev. A 49 (1994) 283.
[24] B.R. Appleton, C. Erginsoy, W.M. Gibson, Phys. Rev. 161 (1967) 330.
[25] J. Hone, B. Batlogg, Z. Benes, A.T. Johnson, J.E. Fischer, Science 289 (2000) 1730.
[26] H. Goldstein, Classical Mechanics, Addison-Wesley, Reading, Massachusetts, 1982. p. 386.
[27] J.U. Andersen, W.M. Augustyniak, E. Uggerhj, Phys. Rev. B 3 (1971) 705.
[28] M.J. Pedersen, J.U. Anderson, W.M. Augustyniak, Radiat. Eff. 12 (1972) 47.
[29] R. Haakenaasen, L.V. Hau, J.A. Golovchenko, J.C. Palathingal, J.P. Peng, P. Asoka-Kumar, K.G. Lynn, Phys. Rev. Lett. 75 (1995) 1650.
[30] M. Ćosić, S. Petrović, N. Nešković, Nucl. Instr. Meth. Phys. Res. Sect. B 330 (2014) 33.
[31] H. Weyl, The Group Theory and Quantum Mechanics, Dover Publications, New York, 1950. p. 93.
[32] M. Born, E. Wolf, Principles of Optics: Electromagnetic Theory of Propagation, Interference and Diffraction of Light, Cambridge University Press, Cambridge, 1999. p. 134.